NANO LETTERS

pubs.acs.org/NanoLett Letter

Enhancing and Mitigating Radiolytic Damage to Soft Matter in Aqueous Phase Liquid-Cell Transmission Electron Microscopy in the Presence of Gold Nanoparticle Sensitizers or Isopropanol Scavengers

Joanna Korpanty, Lucas R. Parent, and Nathan C. Gianneschi*

Cite This: *Nano Lett.* 2021, 21, 1141−1149 Read Online

ACCESS | Metrics & More | Article Recommendations | Supporting Information

ABSTRACT: In this work, we describe the radiolytic environment experienced by a polymer in water during liquid-cell transmission electron microscopy (LCTEM). We examined the radiolytic environment of aqueous solutions of poly(ethylene glycol) (PEG, 2400 g/mol) in the presence of sensitizing gold nanoparticles (GNPs, 100 nm) or radical scavenging isopropanol (IPA). To quantify polymer damage, we employed *post-mortem* analysis via matrix-assisted laser desorption/ionization imaging mass spectrometry (MALDI-IMS). This approach confirms IPA (1−10% w/v) can significantly mitigate radiolysis-induced damage to polymers in water, while GNPs significantly enhance damage. We couple LCTEM experiments with simulations to provide a generalizable strategy for assessing radiolysis mitigation or enhancement. This study highlights the caution required for LCTEM experiments on inorganic nanoparticles where solution phase properties of surrounding organic materials or the solvent itself are under investigation. Furthermore, we anticipate an increased use of scavengers for LCTEM studies of all kinds.

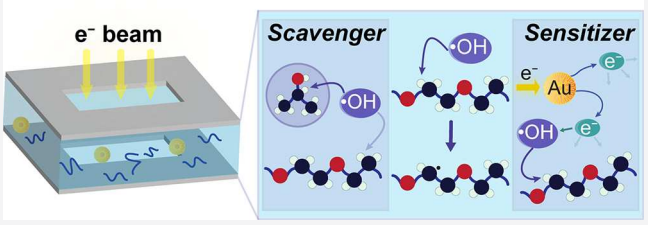

KEYWORDS: *Liquid-Phase TEM, Radical Scavengers, TEM, Polymers, Gold Nanoparticles*

Liquid-cell transmission electron microscopy (LCTEM) is a nascent technique for imaging solvated nanomaterials and their dynamics *in situ* (Figure S1). Though there is a breadth of literature concerned with studying solvated inorganic materials,[1−5] progress in imaging solvated soft matter, either by itself or in hybrid organic−inorganic systems, has been limited.[6−11] Growth in this field has been hindered by the inherently low contrast of soft materials, leading to the use of imaging conditions that cause electron beam-induced damage. More generally, under ionizing radiation, damage to solvated soft materials is chiefly caused by radiolysis of the surrounding solvent, a process that releases reactive species into solution that can undergo secondary reactions with the substrate.[12−14] Underscoring this, recent irradiation studies performed on a series of rigorously dried polymers under γ and electron beam irradiation show negligible change in polymer molecular weight, suggesting solvent radiolysis is indeed responsible for the majority of solvated polymer damage.[15] Moreover, irradiation studies performed on several aqueous polymers have all concluded hydroxyl radicals (•OH) are the main culprits, with hydrogen atoms and hydrated electrons playing a lesser role.[15−22] Thus, by simply adding an alcohol cosolvent that scavenges •OH,[23−25] it should be possible to mitigate indirect damage to soft matter. In the context of LCTEM, adding a scavenging alcohol could relax strict low electron flux (e^{-} Å^{-2} s^{-1}) constraints,[5,6,9−11,26−28] which limit the achievable spatial and temporal resolution. Ultimately, easing these restrictions would expand the diversity of materials and processes that can be readily studied using LCTEM.[29,30] Despite precedents from the field of radiation chemistry, limited work has been reported regarding the exploration of radical scavengers[31−37] to mitigate damage to organic materials in LCTEM.

Though it is well established that soft matter, organic solvents, and water are all sensitive to damage, the susceptibility of solutions containing inorganic materials to beam-induced effects is often overlooked. This is especially true for one of the most routinely studied materials in LCTEM literature: gold nanoparticles (GNPs).[38−44] There has been an assumption that metallic nanoparticles, which are generally highly chemically stable, can be irradiated in LCTEM without regard to radiolysis. In particular, the potential exists for damage to surface ligands or other organic components of the

Received: November 23, 2020
Revised: January 6, 2021
Published: January 15, 2021

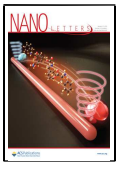

https://dx.doi.org/10.1021/acs.nanolett.0c04636
Nano Lett. 2021, 21, 1141−1149

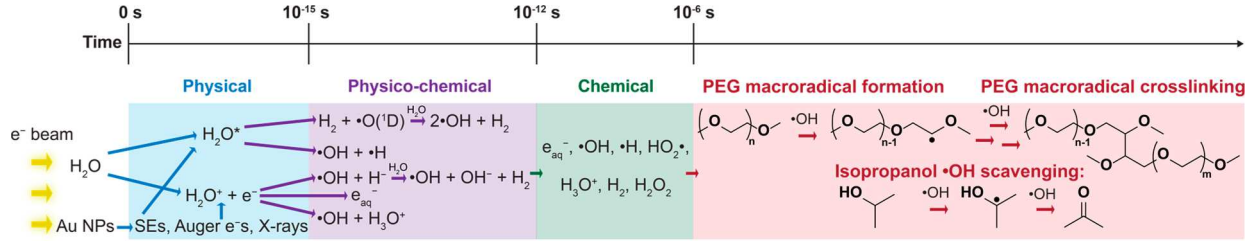

Figure 1. Water radiolysis, PEG secondary reactions, IPA scavenging, and GNP dose enhancement under electron beam irradiation. Note that IPA can scavenge the radicals that cause PEG macroradical formation and cross-linking, whereas GNPs have the opposite effect and act as sensitizers.

system. Indeed, prior radiation chemistry studies have shown GNPs have a significant "dose enhancement" effect in water.[45−55] The sensitization effect of gold, reported to increase the effective dose by nearly 100 times under X-ray radiation,[52,56] is chiefly caused by the irradiation-triggered release of secondary electrons and X-rays from GNPs, which directly radiolyze the surrounding solution, causing an effective local dose increase. Thus, in water, any organic molecule is expected to readily undergo indirect beam-induced damage during LCTEM,[15−21,57] and this chemical damage should be enhanced by GNPs or mitigated by a scavenging alcohol cosolvent.

Despite the ubiquity of GNPs in LCTEM literature, both by themselves as preformed nanocrystals[39−43,45,58] and in the presence of soft materials,[44,59−62] the sensitizing effect of GNPs has not been directly experimentally explored in the context of LCTEM. Furthermore, though scavengers have been used previously in LCTEM,[31−35] there is a lack of fundamental studies dealing with scavengers as aids for imaging soft matter. Accordingly, in this study, we seek to understand the effect of a prototypical •OH scavenger, isopropanol (IPA), and the effect of sensitizing 100 nm GNPs on 2.4 kDa PEG in water, which we use as a proof-of-concept system for LCTEM polymer damage studies. To evaluate beam-induced damage during LCTEM, we employ a combination of *in situ* LCTEM videography and *post-mortem* matrix-assisted laser desorption/ionization imaging mass spectrometry (MALDI-IMS, Figure S2). MALDI-IMS creates a map of mass spectra across liquid-cell chip surfaces after LCTEM that we process using molecular mass signal intensity of PEG to quantify beam-induced damage.[63]

Aiming to guide and understand experimental LCTEM results, we employ kinetic modeling of radiolysis under LCTEM conditions. With and without additives, the model tracks the evolution of aqueous PEG under 300 keV electron beam irradiation using tabulated *G*-values and reaction rate constants for all species involved. While radiation chemistry literature has provided a foundational framework,[64,65] studies modeling the liquid-cell environment have only been rigorously performed in aqueous conditions without substrates.[12] In an attempt to expand this model, we have examined the irradiated liquid-cell environment for purely aqueous PEG and PEG with sensitizing GNPs or scavenging IPA (Figure 1).

The kinetic model, though simple, accurately reflected the results from LCTEM experiments and is amendable by other researchers to contextualize LCTEM data. We establish that the sensitizing effect of 100 nm GNPs causes magnified PEG damage that could be directly observed through LCTEM imaging and *post-mortem* MALDI-IMS. Conversely, we show IPA mitigates PEG damage, likely by scavenging reactive •OH. Though we observed IPA causes beam-induced charging effects during LCTEM, MALDI-IMS confirms this scavenger lessens polymer damage. These results reaffirm the value of exploring different scavengers for combatting beam damage in soft materials and highlight the potential for GNPs to accelerate damage to organic species in LCTEM. As the latter result is likely generalizable to other metallic nanoparticles,[56,66−69] researchers should not overlook the possibility of beam-induced artifacts in studying such materials, especially for routinely studied organic−inorganic hybrid systems, where critical components of the solution, such as capping agents, ligands, surfactants, and indeed the solvent itself, may be damaged to an even greater extent because of the nanoparticles.

When a solution is exposed to ionizing radiation, constituent molecules undergo decomposition via radiolysis (Figure 1).[65] First, in the physical stage, from the onset of radiation up to 10^{-15} s, incident radiation directly interacts with solution molecules via inelastic scattering, causing ionized and excited molecules as well as subexcitation electrons to form. Next, between 10^{-15} and 10^{-12} s, in the physicochemical stage, excited molecules dissipate energy through numerous processes,[70] yielding a set of reactive intermediates. Finally, in the chemical stage, between 10^{-12} and 10^{-6} s, reactive intermediates formed in the previous stage react with each other and the surrounding solution to yield the primary products. The initial yield of each primary product is specified by its *G*-value, the number of molecules created or destroyed per 100 eV of energy deposited at the end of the chemical stage.[64] Note, *G*-values are related to the energy deposited in the solution, whereas the energy deposited per incident electron is given by the stopping power, which accounts for the dose enhancement of GNPs in solution (Figures S3−S7).

The kinetic model we use in this work was inspired by the work of Schneider et al.,[12] who simulated the chemical environment of irradiated water. For the data we present, we assume all substrates and radiolytic species are homogeneously distributed in the liquid-cell and draw qualitative conclusions about the behavior of the irradiated system. Our model tracks reactions between the primary radiolysis products and the substrates under study using tabulated *G*-values, reactions, and associated rate constants (Tables S1−S5). In our model, we assume water has a constant concentration across all systems.[12] We assume water and GNPs are the only species altered by direct radiation, and all other species solely transform through secondary reactions. Finally, we account for the GNP dose enhancement by using concentration-dependent dose enhancement factors (DEFs) measured under MeV electron beam irradiation; we convert these experimental DEFs to theoretical values at 300 keV by conducting calculations with stopping power values at these different energies (Figure S3).[56] We note

https://dx.doi.org/10.1021/acs.nanolett.0c04636
Nano Lett. 2021, 21, 1141−1149

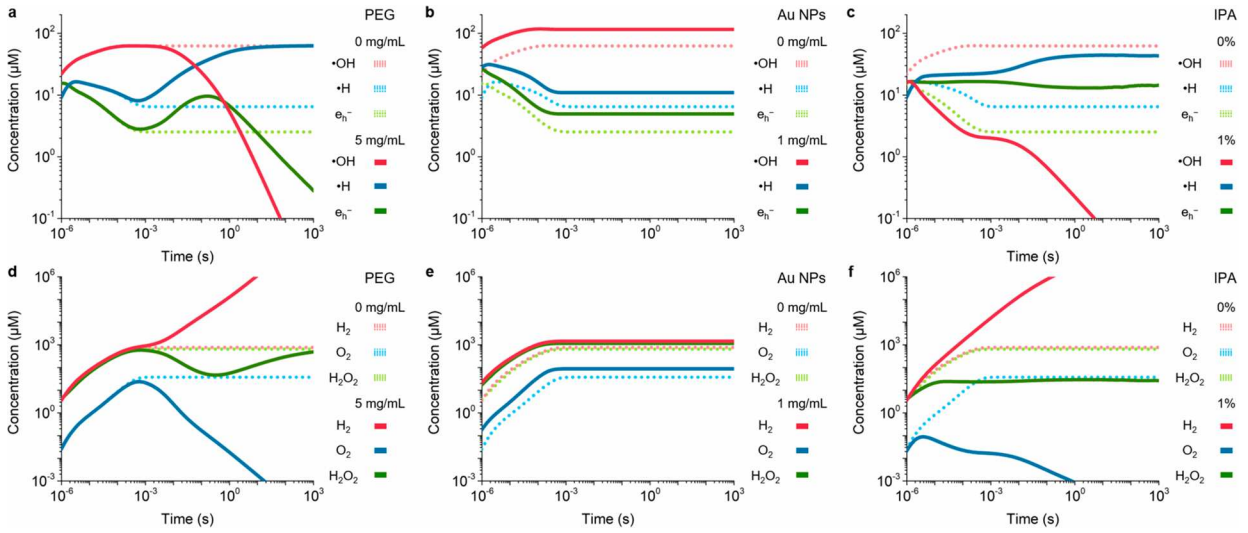

Figure 2. Comparison of the temporal evolution of radical and molecular radiolytic products generated by irradiating deaerated water in the presence of PEG, GNPs, or IPA at 25 °C and pH 7 at a dose rate of 7.5×10^7 Gy/s. (a) Temporal evolution of radical radiolytic products generated from water in the presence of 0 and 5 mg/mL 2.4 kDa PEG, (b) 0 and 1 mg/mL 100 nm GNPs, and (c) 0% and 1% IPA. (d) Temporal evolution of molecular radiolytic products generated from water in the presence of 0 and 5 mg/mL 2.4 kDa PEG, (e) 0 and 1 mg/mL 100 nm GNPs, and (f) 0% and 1% IPA.

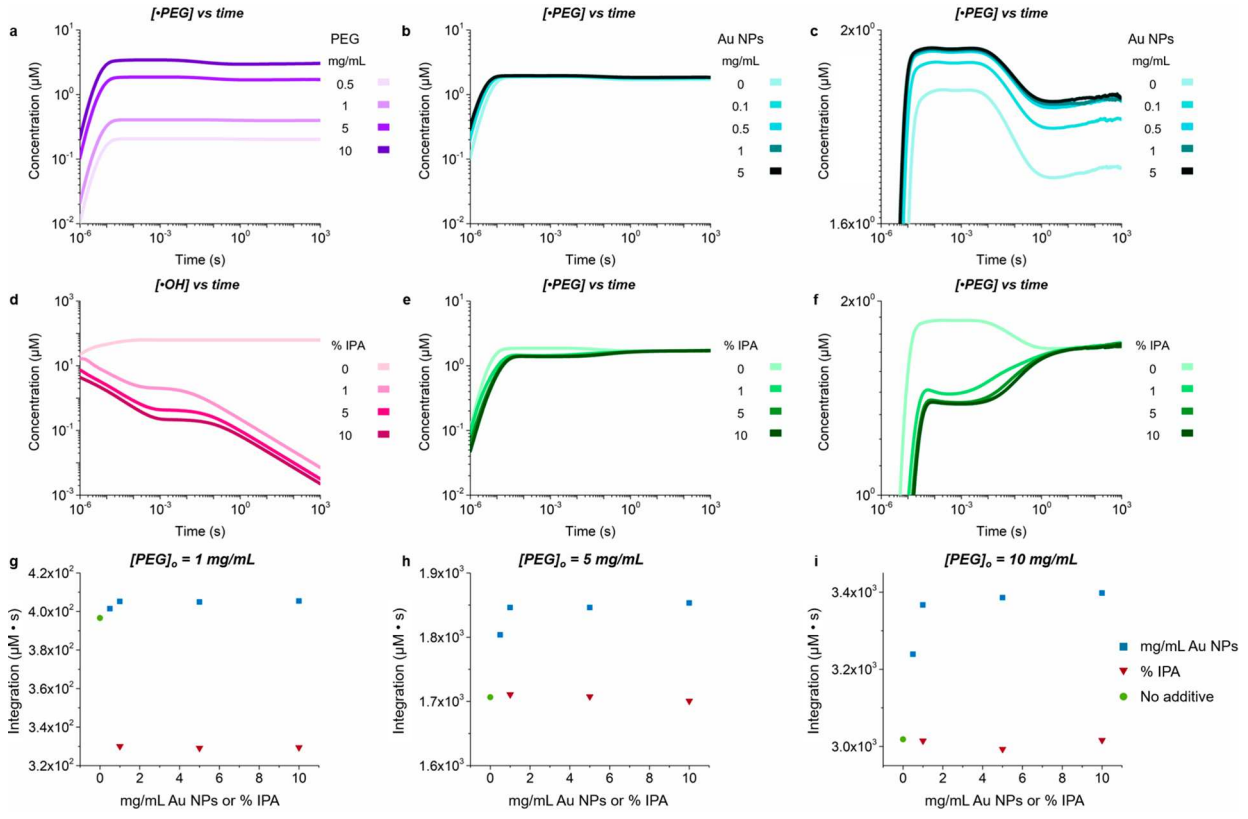

Figure 3. Comparison of the temporal evolution of radiolytic products generated by irradiating deaerated water in the presence of PEG, GNPs, and/or IPA at 25 °C and pH 7 at a dose rate of 7.5×10^7 Gy/s. (a) Temporal evolution of PEG macroradicals generated under varying $[PEG]_o$. (b) Temporal evolution of PEG macroradicals generated under varying $[GNP]_o$ and $[PEG]_o$ fixed at 5 mg/mL. (c) Zoomed in section of plot b. (d) Temporal evolution of •OH generated under varying percentages of IPA cosolvent. (e) Temporal evolution of PEG macroradicals generated under varying percentages of IPA cosolvent and $[PEG]_o$ fixed at 5 mg/mL. (f) Zoomed in section of plot e. Under varying amounts of % IPA or mg/mL GNPs, the curve of $[PEG^•]_t$ vs time was integrated to quantify the amount of damaged polymer chains formed. Initial polymer concentrations of (g) 1 mg/mL, (h) 5 mg/mL, and (i) 10 mg/mL are shown. Note that 0 mg/mL GNPs and 0% IPA are given as the same point for each concentration of $[PEG]_o$.

the DEF of GNPs depends on their size and shape, the distance of solutes from the GNP, and the type and energy of incident radiation.[46−53,71] For simplicity, again, we assume GNPs are distributed in the liquid-cell uniformly so the DEF is

https://dx.doi.org/10.1021/acs.nanolett.0c04636
Nano Lett. 2021, 21, 1141−1149

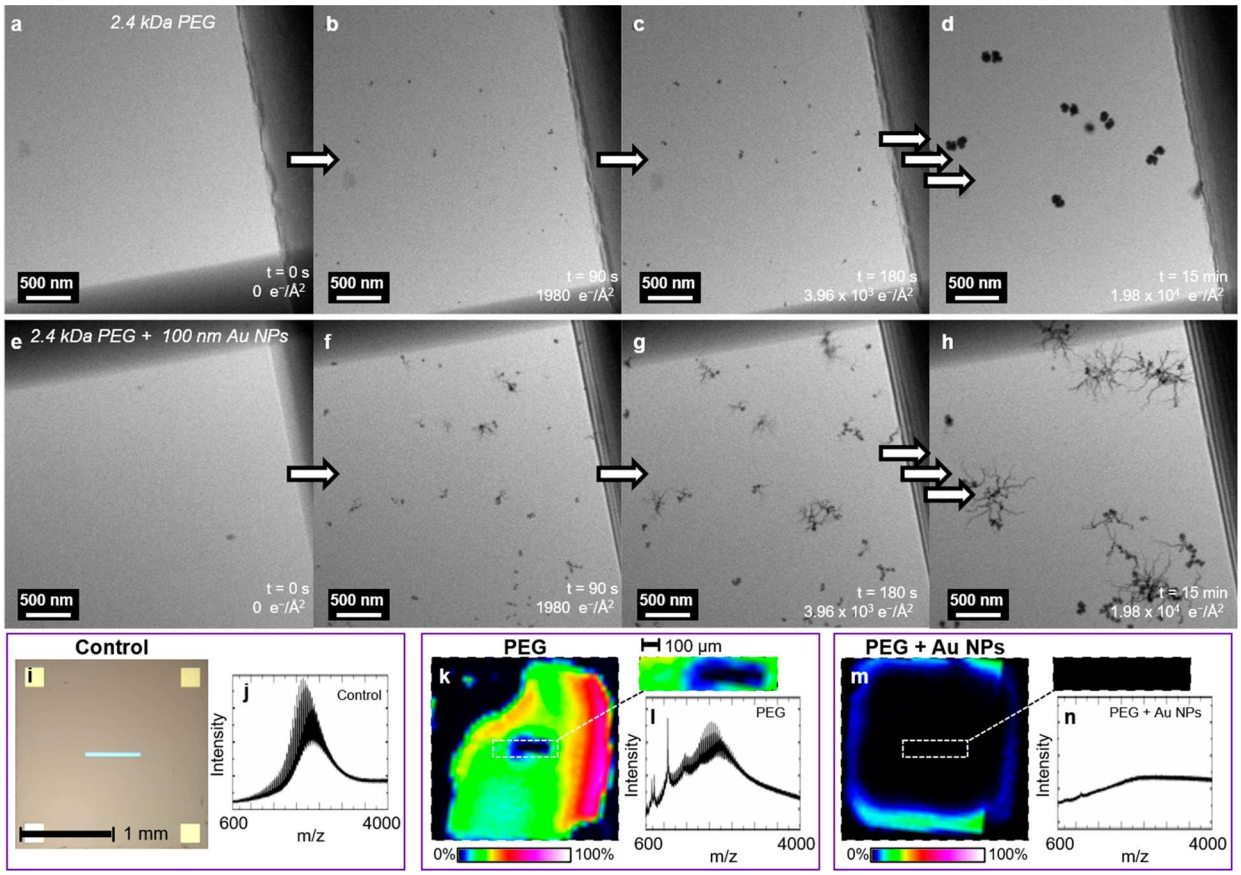

Figure 4. LCTEM and MALDI-IMS data for 5 mg/mL 2.4 kDa PEG imaged in the presence and absence of 0.05 mg/mL 100 nm GNPs. (a)−(d). Single frames of LCTEM video of 5 mg/mL PEG imaged at 22 e^{-} $Å^{-2}$ s^{-1} for 15 min. (e)−(h) Single frames of LCTEM video of 5 mg/mL PEG and 0.05 mg/mL GNPs imaged at 22 e^{-} $Å^{-2}$ s^{-1} for 15 min. (i) Optical image of one of the liquid-cell chips. (j) Mass spectrum of an unimaged chip coated with 5 mg/mL 2.4 kDa PEG. (k) MALDI-IMS color map of chip surface with inset showing the chip window for PEG imaged by LCTEM in the absence of GNPs with a mass filter of 2400 ± 100 m/z displayed as 0−100% of total intensity on a logarithmic scale. (l) Mass spectrum for 2.4 kDa PEG imaged by LCTEM in the absence of 100 nm GNPs. (m) MALDI-IMS color map of chip surface with inset showing window for PEG imaged in the presence of GNPs with a mass filter of 2400 ± 100 m/z displayed as 0−100% of total intensity on a logarithmic scale. (n) Mass spectrum for 2.4 kDa PEG imaged by LCTEM in the presence of 100 nm GNPs.

uniform and we may draw qualitative conclusions using this simple model. Finally, we use LCTEM electron energy-loss spectroscopy (EELS) to verify that an experimental DEF is caused by GNPs in water under 300 keV electron beam irradiation (Figures S8−S15).

First, we examined the radiolytic environment of the liquid-cell in neat, deaerated water and overlaid these data with the behavior of radiolytic species in the presence of the substrate, PEG, and additives, IPA or GNPs (Figure 2). Compared to pure water, adding 5 mg/mL of 2.4k PEG has a significant effect on the temporal evolution of all aqueous radiolytic products (Figure 2a,d).

Next, we introduce 100 nm GNPs into the model at 1 mg/mL, and consistent with radiation chemistry literature,[46,48,51,53,56] GNPs cause increased steady state concentrations for all radiolytic species (Figure 2b,e). With the model predicting that GNPs do impact the temporal evolution of radiolytic products, we next aimed to investigate the effect of IPA as a $^{\bullet}OH$ scavenger. IPA alters the behavior of all radiolytic products and, in particular, significantly lowers $[^{\bullet}OH]$ (Figure 2c,f).

Having confirmed the presence of individual additives alters the temporal evolution of radiolytic species generated from water using our model, we next aimed to understand the effect of having both PEG and an additive in the same liquid-cell. Here, we tracked the evolution of radiolytic products when hydrated PEG is simultaneously irradiated with either GNPs or IPA (Figure S16). Under different initial conditions, we then aimed to track the evolution of $^{\bullet}OH$, the most destructive radiolytic product, and $^{\bullet}PEG$ (Figure 3). First, we studied the effect of varying the initial PEG concentration, $[PEG]_o$, without other additives. As $[PEG]_o$ increases from 0.5 to 10 mg/mL, the steady state concentration of $^{\bullet}PEG$ increases (Figure 3a). Similarly, increasing $[GNPs]_o$ causes a subtle increase in the macroradical steady state concentration with $[PEG]_o$ fixed at 5 mg/mL (Figure 3b,c). We also monitored the evolution of nonradical PEG chains and the formation of damaged polymeric products. We observed that at fixed $[PEG]_o$, a larger fraction of damaged product forms as $[GNP]_o$ increases, with a more pronounced effect at higher $[PEG]_o$ (Figure 3g−i).

With the model predicting that the presence of GNPs does impact the temporal evolution of $^{\bullet}PEG$, we next aimed to evaluate the effect of IPA as a $^{\bullet}OH$ scavenger. Without PEG, adding increasing amounts of IPA causes a significant decrease in $[^{\bullet}OH]$ (Figure 3d). Interestingly, while $^{\bullet}OH$ does not appear to reach a steady state, $^{\bullet}PEG$ reaches roughly the same steady state both with and without IPA, regardless of the

https://dx.doi.org/10.1021/acs.nanolett.0c04636
Nano Lett. 2021, 21, 1141−1149

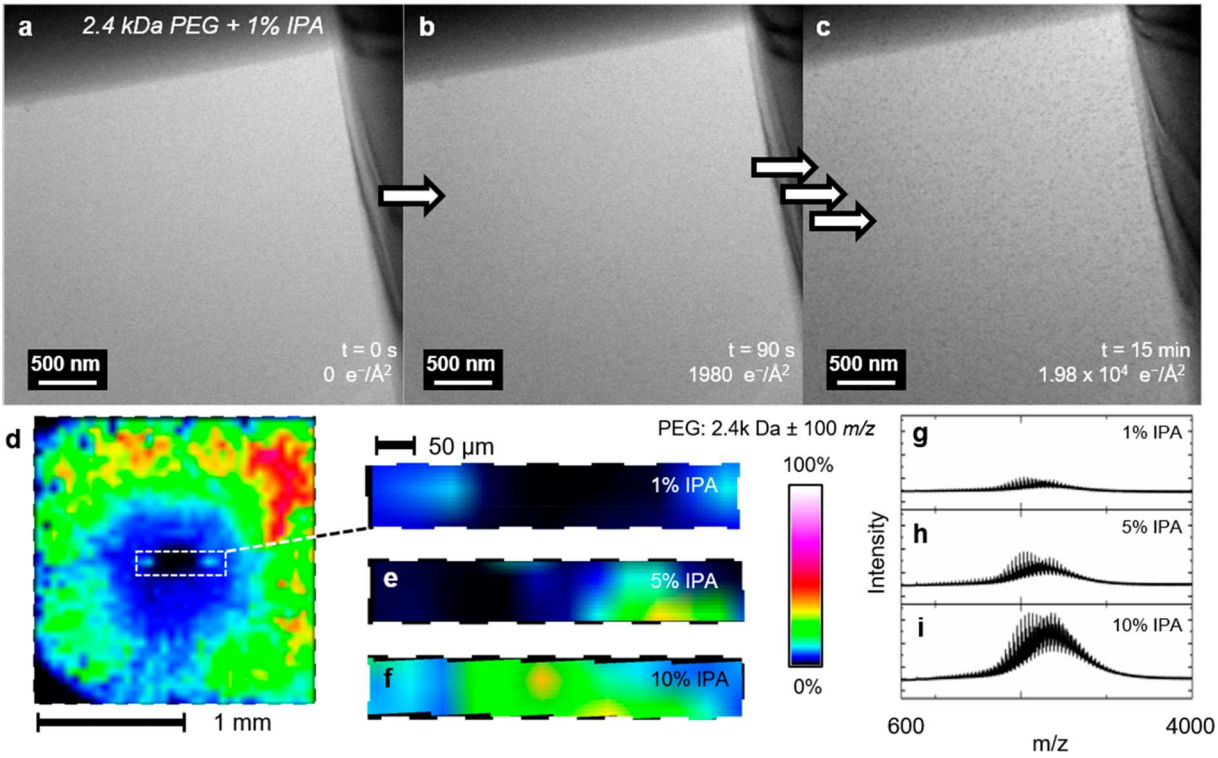

Figure 5. LCTEM and MALDI-IMS data for 5 mg/mL 2.4 kDa PEG imaged in the presence of different percentages of IPA cosolvent. (a)−(c) Single frames of LCTEM video of 5 mg/mL PEG imaged at 22 $e^- Å^{-2} s^{-1}$ for 15 min with 1% IPA cosolvent. (d) MALDI-IMS color map of top chip surface with inset showing window after imaging 2.4 kDa PEG with 1% IPA cosolvent with a mass filter of 2400 ± 100 m/z displayed as 0−100% of total intensity on a logarithmic scale. MALDI-IMS color map of window after imaging 2.4 kDa PEG with (e) 5% IPA cosolvent and (f) 10% IPA cosolvent with a mass filter of 2400 ± 100 m/z displayed as 0−100% of total intensity on a logarithmic scale. Mass spectrum of 5 mg/mL 2.4 kDa PEG imaged by LCTEM with (g) 1% IPA cosolvent, (h) 5% IPA cosolvent, and (i) 10% IPA cosolvent.

percentage of IPA (Figure 3d−f). However, the greatest [•PEG] is reached with 0% IPA, followed by 1% IPA, 5% IPA, and 10% IPA. As the formation of •PEG necessarily causes a change in polymer structure, the greatest damage to PEG should occur without IPA; note, opposite to the effect of GNPs, the damage-reducing effect of IPA is more pronounced at lower $[PEG]_o$ (Figure 3g−i).

With modeled predictions in hand concerning PEG damage enhancement with GNPs during LCTEM, we prepared two samples: 5 mg/mL PEG and 5 mg/mL PEG with 0.05 mg/mL 100 nm GNPs both in water (Figure 4). Aiming to damage PEG, each of the four liquid-cell corners was sequentially irradiated for 15 min uninterrupted at a flux of 22 $e^- Å^{-2} s^{-1}$ at 300 keV, starting with one corner, and in turn moving the beam to each of the other three corners; each corner received a fluence of 19 800 $e^- Å^{-2}$, and the entire liquid-cell received a cumulative fluence of 79 200 $e^- Å^{-2}$. Damage phenomena that manifest in real space images were captured using Camtasia Studio (Figure 4a−h, Videos S1 and S2). Both with and without GNPs, discrete, high-contrast particles proliferated within the irradiated region but with notable differences between the two experiments. Without GNPs, PEG solutions exhibited gradual beam damage during 15 min of continuous imaging in the first corner of the liquid-cell, with negligible damage when imaging each subsequent corner (Figure 4a−d, Figures S17 and S18). Conversely, with GNPs, PEG rapidly formed dendritic structures on the GNPs within seconds (Figure 4e−h, Figures S19 and S20, Videos S1 and S2). The resulting structures moved rapidly, likely from charge accumulation and electric field production in the irradiated region.[5,72] Unlike the GNP-free system, damage phenomena manifested similarly in each irradiated corner (Figures S17 and S18).

For *post-mortem* MALDI-IMS analysis, we evaluated the used liquid-cell chips, a pair of top and bottom chips, for each sample as well as a control chip, which was prepared without exposure to LCTEM irradiation. The unimaged control chip was coated with 5 mg/mL 2.4k PEG, the same concentration used for LCTEM. MALDI-IMS mass spectra and color maps reveal that PEG irradiated during LCTEM in both experiments has a far lower mass signal intensity than the control, indicating radiolysis-induced PEG damage (Figure 4j−n). However, comparing the two irradiated samples reveals that GNPs cause a detectable increase in PEG damage; with GNPs present, the PEG signal was completely obliterated in the imaged window, generating a spectrum lacking discrete fragments (Figure 4l,n). Note, lower m/z peaks now visible correspond to the MALDI matrix (Figure 4l, Figure S21). At a fixed flux, more PEG survived when imaged in the absence of GNPs, with discrete peaks of the polymer distribution remaining. In the GNP system, LCTEM videographic data qualitatively indicate heterogeneous GNP sensitization, where the local dose within ca. 20 nm of a GNP is significantly higher than in the surrounding solution, causing localized PEG damage at GNPs (Figure 4, Video S2).[73] These two experiments, imaging PEG with and without GNPs, were repeated at a lower flux of 9 $e^- Å^{-2} s^{-1}$ and 300 keV; again, as predicted by modeling, MALDI-IMS data show there is a lower signal intensity for the sample containing GNPs, though more PEG survives in these two respective systems at reduced flux

https://dx.doi.org/10.1021/acs.nanolett.0c04636
Nano Lett. 2021, 21, 1141−1149

(Figure S21 and Videos S3 and S4). Note, control experiments of unimaged samples show that GNPs do not impact the ability of PEG to ionize by MALDI, indicating that the MALDI detection sensitivity for PEG is consistent across experiments (Figure S22). These LCTEM and MALDI-IMS results confirm that, at a fixed flux and $[PEG]_o$, GNPs exhibit a sensitizing effect that causes more rapid and more net polymer damage, as evidenced by lower signal intensity for the polymer and rapid formation of damaged, dendritic polymer products at GNP surfaces (Figure 4e−h). Note that though we employ a 300 keV electron beam in our experiments, radiolysis should be reduced at higher beam energies and so we expect PEG to undergo more radiolytic damage at lower accelerating voltages.[29] Moreover, this enhanced damage at lower accelerating voltages should be further magnified in the presence of GNPs, following the same trend as 300 keV electron beam irradiation. The increase in radiolysis with decreased accelerating voltage can be rationalized by the increase in stopping power values of water and gold at lower accelerating voltages; at 300 keV, the stopping power of water is 2.360 $(MeV{\cdot}cm^2)/g$ and of gold is 1.274 $(MeV{\cdot}cm^2)/g$, whereas at 80 keV, the stopping power of water is 4.761 $(MeV{\cdot}cm^2)/g$ and of gold is 2.327 $(MeV{\cdot}cm^2)/g$.[74]

For LCTEM studies investigating to what extent damage is reduced with IPA, three samples were prepared, each with 5 mg/mL of PEG and 1%, 5%, or 10% IPA. Using the same protocol as previous experiments, each liquid-cell was imaged for 15 min uninterrupted at each corner at a flux of 22 $e^- Å^{-2} s^{-1}$ (Figure 5, Figures S22−S24). The proliferation of damaged products in the irradiated region is seen for all three experiments, in a form of damage distinct from purely aqueous PEG. Due to the lower dielectric constant of IPA, higher percentages of IPA led to more charging phenomena.[58] Notably, material was drawn into irradiated regions rapidly with 5% and 10% IPA and less so with 1% (Figure 5a−c, Figures S22−S24, Videos S5, S6, and S7). However, visual observation of material accumulation is not necessarily indicative of damage. To assess polymer damage, MALDI-IMS was again used to probe the liquid-cell chips following LCTEM. Critically, MALDI-IMS data reveal that IPA was effective in mitigating PEG damage, with increasing retention of PEG signal intensity from 1% to 5% to 10% IPA (Figure 5g−i). While modeling predicts little effect from IPA at 5 mg/mL PEG, due to local depletion of precursors and limited diffusion, we find experimental LCTEM and MALDI-IMS data to be more consistent with trends modeled for lower $[PEG]_o$ (Figure 3g−i). Despite the agreement between modeling and experimental data, in LCTEM, damage mitigation comes with increased charging. Such charging phenomena are caused by inelastic scattering of electrons, leading to the formation of secondary and Auger electrons, which then escape from the sample.[13] Since IPA has a lower dielectric constant than water, a mixture of the two solvents is not able to dissipate this buildup of charge as well as pure water, leading to a charge imbalance and thus real space charging phenomena. Though charging is not necessarily indicative of radiolytic damage to the solvent or solvated species,[72] it is an undesired beam−sample interaction that cannot be studied using our simple kinetic model; charging is highly sample-dependent, reflecting the magnitude of inelastic scattering interactions between the electron beam and the entire liquid-cell, including the solvent, solvated species, and silicon nitride windows. Despite complications from charging, our results show scavengers can mitigate damage, and scavengers with different charging behaviors, but with efficiencies similar to that of IPA, should be explored. Once again, we expect enhanced radiolytic damage at lower accelerating voltages and so, at a fixed concentration of PEG and IPA, we expect PEG to undergo more damage at lower beam energies. We also note that while radiolytic damage to PEG can be mitigated by the addition of a scavenger, it is possible that polymer design[75,76] can also limit beam damage; for instance, an aromatic polymer should show enhanced stability compared to the sterically unhindered, heteroatom-containing backbone of PEG.[15,19]

To calibrate *post-mortem* MALDI-IMS results, we conducted MALDI for mixtures containing different percentages of low and high molecular weight PEG. These data reveal the lower molecular weight polymer produces a more intense signal even when the larger polymer composes up to 99% of the sample (Figure S25). This may explain why MALDI signal intensity is reduced when the polymer undergoes damage, but no new peaks appear in the mass spectra, as cross-linking is the predominant $^{\bullet}$PEG quenching reaction in LCTEM. Moreover, a heavily cross-linked polymer, such as the dense particles produced under LCTEM irradiation, likely cannot ionize as easily as a linear, nonaggregated polymer to produce a MALDI signal. PEG may also undergo scission, forming fragments that are likely obscured by low molecular weight matrix peaks, though scission is expected to be the less favored damage mechanism given the flexibility and low steric hindrance of the PEG heteroatom-containing backbone (Figure S25).[15,19]

In summary, using a multimodal approach of modeling combined with *in situ* imaging and *post-mortem* mass spectrometry, we show LCTEM conditions and samples can be tuned to effectively image solvated polymers, while raising relevant questions about the survivability of soft materials, including surface ligands, surfactants, and so on, imaged with GNPs, especially at routinely employed fluxes for imaging GNPs.[77−80] The sensitizing effect of GNPs should be generalizable to all metallic NPs. Therefore, such inorganic species should be studied with soft materials at far lower fluxes than currently in use for even soft matter alone (<1 $e^- Å^{-2} s^{-1}$ and <10 $e^- Å^{-2}$). Furthermore, these studies should be conducted with *post-mortem* validation of the soft matter component.[6,10,11,26,63] Lower fluxes are of course possible for high contrast materials, although this would preclude any attempt at achieving lattice resolution. The caveat is studies on dissolution, etching, and destruction, where significant and fruitful mechanistic studies of particle geometry and facets have been conducted.[37,77−79]

In addition to demonstrating limitations of LCTEM for organic−inorganic hybrid systems, we suggest $^{\bullet}$OH scavengers as a solution for low flux constraints of LCTEM when imaging soft materials. We test IPA as a $^{\bullet}$OH scavenger and prove by MALDI-IMS that it mitigates polymer damage. Though high concentrations of IPA exacerbate beam-induced charging effects, we believe other $^{\bullet}$OH scavengers should be explored. Such fundamental and systematic scavenger studies would allow LCTEM to continue to become increasingly reliable and robust for soft matter characterization.

Finally, the kinetic model presented in this work can be tailored by researchers to predict or rationalize their own LCTEM results. We stress the importance of verifying both modeling and LCTEM data by employing a complementary *post-mortem* technique suited to the material under inves-

https://dx.doi.org/10.1021/acs.nanolett.0c04636
Nano Lett. 2021, 21, 1141−1149

tigation, such as MALDI-IMS for polymers and biomolecules,[63] or diffraction for crystalline materials.[10,81]

■ ASSOCIATED CONTENT

Supporting Information

The Supporting Information is available free of charge at https://pubs.acs.org/doi/10.1021/acs.nanolett.0c04636.

LCTEM data of PEG imaged at 22 e^- $Å^{-2}$ s^{-1} at 90x speed (AVI)

LCTEM data of PEG imaged with GNPs at 22 e^- $Å^{-2}$ s^{-1} at 90x speed (AVI)

LCTEM data of PEG imaged at 9 e^- $Å^{-2}$ s^{-1} at 90x speed (AVI)

LCTEM data of PEG imaged with GNPs at 9 e^- $Å^{-2}$ s^{-1} at 90x speed (AVI)

LCTEM data of PEG imaged with 1% IPA at 22 e^- $Å^{-2}$ s^{-1} at 90x speed (AVI)

LCTEM data of PEG imaged with 5% IPA at 22 e^- $Å^{-2}$ s^{-1} at 90x speed (AVI)

LCTEM data of PEG imaged with 10% IPA at 22 e^- $Å^{-2}$ s^{-1} at 90x speed (AVI)

Sample preparation, LCTEM experimental details, MALDI-IMS experimental details, kinetic modeling details, additional LCTEM, MALDI, and kinetic modeling with supporting figures, and EELS data with supporting figures (PDF)

■ AUTHOR INFORMATION

Corresponding Author

Nathan C. Gianneschi − *Department of Chemistry, International Institute for Nanotechnology, Chemistry of Life Processes Institute, Simpson Querrey Institute and Department of Materials Science & Engineering, Department of Biomedical Engineering and Department of Pharmacology, Northwestern University, Evanston, Illinois 60208, United States;* orcid.org/0000-0001-9945-5475; Email: nathan.gianneschi@northwestern.edu

Authors

Joanna Korpanty − *Department of Chemistry, International Institute for Nanotechnology, Chemistry of Life Processes Institute, Simpson Querrey Institute, Northwestern University, Evanston, Illinois 60208, United States;* orcid.org/0000-0002-9274-5936

Lucas R. Parent − *Innovation Partnership Building, University of Connecticut, Storrs, Connecticut 06269, United States*

Complete contact information is available at: https://pubs.acs.org/10.1021/acs.nanolett.0c04636

Author Contributions

J.K. and N.C.G. devised the project. J.K. performed LCTEM, MALDI-IMS, and MATLAB modeling and drafted the paper. L.R.P. performed EELS measurements. All authors wrote and edited the manuscript. All authors have given approval to the final version of the manuscript.

Notes

The authors declare no competing financial interest.

■ ACKNOWLEDGMENTS

Research in the Gianneschi group was conducted with government support under and awarded by DoD through the ARO (W911NF-17-1-0326). In addition, the authors thank the NSF for support of both the Parent and Gianneschi groups through a joint research grant (CHE-MSN 1905270). This research used EPIC facility of Northwestern University's NUANCE Center, which has received support from the Soft and Hybrid Nanotechnology Experimental (SHyNE) Resource (NSF ECCS-1542205), the MRSEC program (NSF DMR1720139) at the Materials Research Center, the International Institute for Nanotechnology (IIN), the Keck Foundation, and the State of Illinois, through the IIN. This work also made use of the IMSERC at Northwestern University, which has received support from the Soft and Hybrid Nanotechnology Experimental (SHyNE) Resource (NSF ECCS-1542205), the State of Illinois, and the International Institute for Nanotechnology (IIN).

■ ABBREVIATIONS

LCTEM, liquid-cell transmission electron microscopy; PEG, poly(ethylene glycol); GNPs, gold nanoparticles; IPA, isopropanol; MALDI-IMS, matrix-assisted laser desorption imaging mass spectrometry; EELS, electron energy-loss spectroscopy

■ REFERENCES

(1) Nielsen, M. H.; Aloni, S.; De Yoreo, J. J. In situ TEM imaging of CaCO3 nucleation reveals coexistence of direct and indirect pathways. *Science* **2014**, *345* (6201), 1158−1162.

(2) Wang, T.; Lu, W.; Yang, Q.; Li, S.; Yu, X.; Qiu, J.; Xu, X.; Yu, S. F. In Situ Observation of Nucleation and Crystallization of a Single Nanoparticle in Transparent Media. *J. Phys. Chem. C* **2020**, *124* (28), 15533−15540.

(3) Woehl, T. J.; Evans, J. E.; Arslan, I.; Ristenpart, W. D.; Browning, N. D. Direct in Situ Determination of the Mechanisms Controlling Nanoparticle Nucleation and Growth. *ACS Nano* **2012**, *6* (10), 8599−8610.

(4) de Jonge, N.; Ross, F. M. Electron microscopy of specimens in liquid. *Nat. Nanotechnol.* **2011**, *6* (11), 695−704.

(5) Ross, F. M. Opportunities and challenges in liquid cell electron microscopy. *Science* **2015**, *350* (6267), aaa9886.

(6) Proetto, M. T.; Rush, A. M.; Chien, M.-P.; Abellan Baeza, P.; Patterson, J. P.; Thompson, M. P.; Olson, N. H.; Moore, C. E.; Rheingold, A. L.; Andolina, C.; Millstone, J.; Howell, S. B.; Browning, N. D.; Evans, J. E.; Gianneschi, N. C. Dynamics of Soft Nanomaterials Captured by Transmission Electron Microscopy in Liquid Water. *J. Am. Chem. Soc.* **2014**, *136* (4), 1162−1165.

(7) Wu, H.; Friedrich, H.; Patterson, J. P.; Sommerdijk, N.; de Jonge, N. Liquid-Phase Electron Microscopy for Soft Matter Science and Biology. *Adv. Mater.* **2020**, *32* (25), e2001582.

(8) Gnanasekaran, K.; Chang, H.; Smeets, P. J. M.; Korpanty, J.; Geiger, F. M.; Gianneschi, N. C. In Situ Ni2+ Stain for Liposome Imaging by Liquid-Cell Transmission Electron Microscopy. *Nano Lett.* **2020**, *20* (6), 4292−4297.

(9) Parent, L. R.; Bakalis, E.; Ramírez-Hernández, A.; Kammeyer, J. K.; Park, C.; de Pablo, J.; Zerbetto, F.; Patterson, J. P.; Gianneschi, N. C. Directly Observing Micelle Fusion and Growth in Solution by Liquid-Cell Transmission Electron Microscopy. *J. Am. Chem. Soc.* **2017**, *139* (47), 17140−17151.

(10) Smith, B. J.; Parent, L. R.; Overholts, A. C.; Beaucage, P. A.; Bisbey, R. P.; Chavez, A. D.; Hwang, N.; Park, C.; Evans, A. M.; Gianneschi, N. C.; Dichtel, W. R. Colloidal Covalent Organic Frameworks. *ACS Cent. Sci.* **2017**, *3* (1), 58−65.

(11) Touve, M. A.; Figg, C. A.; Wright, D. B.; Park, C.; Cantlon, J.; Sumerlin, B. S.; Gianneschi, N. C. Polymerization-Induced Self-Assembly of Micelles Observed by Liquid Cell Transmission Electron Microscopy. *ACS Cent. Sci.* **2018**, *4* (5), 543−547.

(12) Schneider, N. M.; Norton, M. M.; Mendel, B. J.; Grogan, J. M.; Ross, F. M.; Bau, H. H. Electron−Water Interactions and Implications

for Liquid Cell Electron Microscopy. *J. Phys. Chem. C* **2014**, *118* (38), 22373−22382.
(13) Woehl, T. J.; Jungjohann, K. L.; Evans, J. E.; Arslan, I.; Ristenpart, W. D.; Browning, N. D. Experimental procedures to mitigate electron beam induced artifacts during in situ fluid imaging of nanomaterials. *Ultramicroscopy* **2013**, *127*, 53−63.
(14) Parent, L. R.; Bakalis, E.; Proetto, M.; Li, Y.; Park, C.; Zerbetto, F.; Gianneschi, N. C. Tackling the Challenges of Dynamic Experiments Using Liquid-Cell Transmission Electron Microscopy. *Acc. Chem. Res.* **2018**, *51* (1), 3−11.
(15) Sedláček, O.; Kucka, J.; Monnery, B. D.; Slouf, M.; Vetrik, M.; Hoogenboom, R.; Hruby, M. The effect of ionizing radiation on biocompatible polymers: From sterilization to radiolysis and hydrogel formation. *Polym. Degrad. Stab.* **2017**, *137*, 1−10.
(16) Janik, I.; Ulanski, P.; Hildenbrand, K.; Rosiak, J. M.; von Sonntag, C. Hydroxyl-radical-induced reactions of poly(vinyl methyl ether): a pulse radiolysis, EPR and product study in deoxygenated and oxygenated aqueous solutions. *Journal of the Chemical Society, Perkin Transactions 2* **2000**, *10*, 2041−2048.
(17) Kornacka, E. M. Radiation-induced oxidation of polymers. *Applications of Ionizing Radiation in Materials Processing*; Institute of Nuclear Chemistry and Technology, 2017; pp 184−192.
(18) Kozicki, M.; Kujawa, P.; Rosiak, J. M. Pulse radiolysis study of diacrylate macromonomer in aqueous solution. *Radiat. Phys. Chem.* **2002**, *65* (2), 133−139.
(19) Sedláček, O.; Černoch, P.; Kučka, J.; Konefal, R.; Štěpánek, P.; Vetrík, M.; Lodge, T. P.; Hrubý, M. Thermoresponsive Polymers for Nuclear Medicine: Which Polymer Is the Best? *Langmuir* **2016**, *32* (24), 6115−6122.
(20) Ulanski, P.; Bothe, E.; Hildenbrand, K.; Rosiak, J. M.; von Sonntag, C. Hydroxyl-radical-induced reactions of poly(acrylic acid); a pulse radiolysis, EPR and product study. Part I. Deoxygenated aqueous solutions. *J. Chem. Soc., Perkin Trans. 2* **1996**, *1*, 13−22.
(21) von Sonntag, C. Free-radical-induced chain scission and cross-linking of polymers in aqueous solution—an overview. *Radiat. Phys. Chem.* **2003**, *67* (3), 353−359.
(22) Kujawa, P.; Mohid, N.; Zaman, K.; Manshol, W.; Ulanski, P.; Rosiak, J. M. Pulse radiolysis of butyl acrylate in aqueous solution. *Radiat. Phys. Chem.* **1998**, *53* (4), 403−409.
(23) Cederbaum, A. I.; Qureshi, A.; Cohen, G. Production of formaldehyde and acetone by hydroxyl-radical generating systems during the metabolism of tertiary butyl alcohol. *Biochem. Pharmacol.* **1983**, *32* (23), 3517−3524.
(24) Lloyd, A. C.; Darnall, K. R.; Winer, A. M.; Pitts, J. N. Relative rate constants for the reactions of OH radicals with isopropyl alcohol, diethyl and DI-n-propyl ether at 305 ± 2 K. *Chem. Phys. Lett.* **1976**, *42* (2), 205−209.
(25) Mincher, B. J.; Arbon, R. E.; Knighton, W. B.; Meikrantz, D. H. Gamma-ray-induced degradation of PCBs in neutral isopropanol using spent reactor fuel. *Appl. Radiat. Isot.* **1994**, *45* (8), 879−887.
(26) Jiang, N.; Spence, J. C. H. On the dose-rate threshold of beam damage in TEM. *Ultramicroscopy* **2012**, *113*, 77−82.
(27) Gnanasekaran, K.; Chang, H.; Smeets, P. J. M.; Korpanty, J.; Geiger, F. M.; Gianneschi, N. C. In Situ Ni2+ Stain for Liposome Imaging by Liquid-Cell Transmission Electron Microscopy. *Nano Lett.* **2020**, *20*, 4292.
(28) Lyu, J.; Gong, X.; Lee, S.-J.; Gnanasekaran, K.; Zhang, X.; Wasson, M. C.; Wang, X.; Bai, P.; Guo, X.; Gianneschi, N. C.; Farha, O. K. Phase Transitions in Metal−Organic Frameworks Directly Monitored through In Situ Variable Temperature Liquid-Cell Transmission Electron Microscopy and In Situ X-ray Diffraction. *J. Am. Chem. Soc.* **2020**, *142* (10), 4609−4615.
(29) de Jonge, N.; Houben, L.; Dunin-Borkowski, R. E.; Ross, F. M. Resolution and aberration correction in liquid cell transmission electron microscopy. *Nature Reviews Materials* **2019**, *4* (1), 61−78.
(30) de Jonge, N. Theory of the spatial resolution of (scanning) transmission electron microscopy in liquid water or ice layers. *Ultramicroscopy* **2018**, *187*, 113−125.
(31) Sutter, E.; Jungjohann, K.; Bliznakov, S.; Courty, A.; Maisonhaute, E.; Tenney, S.; Sutter, P. In situ liquid-cell electron microscopy of silver−palladium galvanic replacement reactions on silver nanoparticles. *Nat. Commun.* **2014**, *5* (1), 4946.
(32) Cho, H.; Jones, M. R.; Nguyen, S. C.; Hauwiller, M. R.; Zettl, A.; Alivisatos, A. P. The Use of Graphene and Its Derivatives for Liquid-Phase Transmission Electron Microscopy of Radiation-Sensitive Specimens. *Nano Lett.* **2017**, *17* (1), 414−420.
(33) Meijerink, M. J.; Spiga, C.; Hansen, T. W.; Damsgaard, C. D.; de Jong, K. P.; Zečević, J. Nanoscale Imaging and Stabilization of Silica Nanospheres in Liquid Phase Transmission Electron Microscopy. *Particle & Particle Systems Characterization* **2019**, *36* (1), 1800374.
(34) Meijerink, M. J.; de Jong, K. P.; Zečević, J. Assessment of oxide nanoparticle stability in liquid phase transmission electron microscopy. *Nano Res.* **2019**, *12* (9), 2355−2363.
(35) Wang, M.; Park, C.; Woehl, T. J. Quantifying the Nucleation and Growth Kinetics of Electron Beam Nanochemistry with Liquid Cell Scanning Transmission Electron Microscopy. *Chem. Mater.* **2018**, *30* (21), 7727−7736.
(36) Wang, M.; Dissanayake, T. U.; Park, C.; Gaskell, K.; Woehl, T. J. Nanoscale Mapping of Nonuniform Heterogeneous Nucleation Kinetics Mediated by Surface Chemistry. *J. Am. Chem. Soc.* **2019**, *141* (34), 13516−13524.
(37) Woehl, T. J. Metal Nanocrystal Formation during Liquid Phase Transmission Electron Microscopy: Thermodynamics and Kinetics of Precursor Conversion, Nucleation, and Growth. *Chem. Mater.* **2020**, *32* (18), 7569−7581.
(38) Grogan, J. M.; Rotkina, L.; Bau, H. H. In situ liquid-cell electron microscopy of colloid aggregation and growth dynamics. *Phys. Rev. E* **2011**, *83* (6), 061405.
(39) Park, J. H.; Schneider, N. M.; Grogan, J. M.; Reuter, M. C.; Bau, H. H.; Kodambaka, S.; Ross, F. M. Control of Electron Beam-Induced Au Nanocrystal Growth Kinetics through Solution Chemistry. *Nano Lett.* **2015**, *15* (8), 5314−5320.
(40) Zhu, C.; Liang, S.; Song, E.; Zhou, Y.; Wang, W.; Shan, F.; Shi, Y.; Hao, C.; Yin, K.; Zhang, T. In-situ liquid cell transmission electron microscopy investigation on oriented attachment of gold nanoparticles. *Nat. Commun.* **2018**, *9* (1), 421.
(41) Zhang, Y.; Keller, D.; Rossell, M. D.; Erni, R. Formation of Au nanoparticles in liquid cell transmission electron microscopy: from a systematic study to engineered nanostructures. *Chem. Mater.* **2017**, *29* (24), 10518−10525.
(42) Hutzler, A.; Fritsch, B.; Jank, M. P.; Branscheid, R.; Martens, R. C.; Spiecker, E.; März, M. Nanoparticles: In Situ Liquid Cell TEM Studies on Etching and Growth Mechanisms of Gold Nanoparticles at a Solid−Liquid−Gas Interface (Adv. Mater. Interfaces 20/2019). *Adv. Mater. Interfaces* **2019**, *6* (20), 1970126.
(43) Meijerink, M. J.; de Jong, K. P.; Zečevic′, J. Growth of Supported Gold Nanoparticles in Aqueous Phase Studied by in Situ Transmission Electron Microscopy. *J. Phys. Chem. C* **2020**, *124* (3), 2202−2212.
(44) Chen, Q.; Smith, J. M.; Park, J.; Kim, K.; Ho, D.; Rasool, H. I.; Zettl, A.; Alivisatos, A. P. 3D motion of DNA-Au nanoconjugates in graphene liquid cell electron microscopy. *Nano Lett.* **2013**, *13* (9), 4556−4561.
(45) Akar, B.; Pushpavanam, K.; Narayanan, E.; Rege, K.; Heys, J. J. Mechanistic investigation of radiolysis-induced gold nanoparticle formation for radiation dose prediction. *Biomedical Physics & Engineering Express* **2018**, *4* (6), 065011.
(46) Cho, S. H. Estimation of tumour dose enhancement due to gold nanoparticles during typical radiation treatments: a preliminary Monte Carlo study. *Phys. Med. Biol.* **2005**, *50* (15), N163−N173.
(47) Gilles, M.; Brun, E.; Sicard-Roselli, C. Quantification of hydroxyl radicals and solvated electrons produced by irradiated gold nanoparticles suggests a crucial role of interfacial water. *J. Colloid Interface Sci.* **2018**, *525*, 31−38.

https://dx.doi.org/10.1021/acs.nanolett.0c04636
Nano Lett. 2021, 21, 1141−1149

(48) Jones, B. L.; Krishnan, S.; Cho, S. H. Estimation of microscopic dose enhancement factor around gold nanoparticles by Monte Carlo calculations. *Med. Phys.* **2010**, *37*, 3809−3816.
(49) Lechtman, E.; Mashouf, S.; Chattopadhyay, N.; Keller, B.; Lai, P.; Cai, Z.; Reilly, R.; Pignol, J. A Monte Carlo-based model of gold nanoparticle radiosensitization accounting for increased radiobiological effectiveness. *Phys. Med. Biol.* **2013**, *58* (10), 3075.
(50) Lin, Y.; McMahon, S. J.; Scarpelli, M.; Paganetti, H.; Schuemann, J. Comparing gold nano-particle enhanced radiotherapy with protons, megavoltage photons and kilovoltage photons: a Monte Carlo simulation. *Phys. Med. Biol.* **2014**, *59* (24), 7675.
(51) Mesbahi, A.; Jamali, F.; Garehaghaji, N. Effect of photon beam energy, gold nanoparticle size and concentration on the dose enhancement in radiation therapy. *Bioimpacts* **2013**, *3* (1), 29−35.
(52) Regulla, D.; Hieber, L.; Seidenbusch, M. Physical and biological interface dose effects in tissue due to X-ray-induced release of secondary radiation from metallic gold surfaces. *Radiat. Res.* **1998**, *150* (1), 92−100.
(53) Tran, H. N.; Karamitros, M.; Ivanchenko, V. N.; Guatelli, S.; McKinnon, S.; Murakami, K.; Sasaki, T.; Okada, S.; Bordage, M. C.; Francis, Z.; El Bitar, Z.; Bernal, M. A.; Shin, J. I.; Lee, S. B.; Barberet, P.; Tran, T. T.; Brown, J. M. C.; Nhan Hao, T. V.; Incerti, S. Geant4Monte Carlo simulation of absorbed dose and radiolysis yields enhancement from a gold nanoparticle under MeV proton irradiation. *Nucl. Instrum. Methods Phys. Res., Sect. B* **2016**, *373*, 126−139.
(54) Rahman, W. N.; Bishara, N.; Ackerly, T.; He, C. F.; Jackson, P.; Wong, C.; Davidson, R.; Geso, M. Enhancement of radiation effects by gold nanoparticles for superficial radiation therapy. *Nanomedicine* **2009**, *5* (2), 136−142.
(55) Mehrnia, S. S.; Hashemi, B.; Mowla, S. J.; Arbabi, A. Enhancing the effect of 4MeV electron beam using gold nanoparticles in breast cancer cells. *Physica Medica* **2017**, *35*, 18−24.
(56) Hossain, M.; Su, M. Nanoparticle Location and Material-Dependent Dose Enhancement in X-ray Radiation Therapy. *J. Phys. Chem. C* **2012**, *116* (43), 23047−23052.
(57) von Sonntag, C.; Bothe, E.; Ulanski, P.; Adhikary, A. Radical transfer reactions in polymers. *Radiat. Phys. Chem.* **1999**, *55* (5−6), 599−603.
(58) Welling, T. A. J.; Sadighikia, S.; Watanabe, K.; Grau-Carbonell, A.; Bransen, M.; Nagao, D.; van Blaaderen, A.; van Huis, M. A. Observation of Undamped 3D Brownian Motion of Nanoparticles Using Liquid-Cell Scanning Transmission Electron Microscopy. *Part. Part. Syst. Charact.* **2020**, *37* (6), 2000003.
(59) Jungjohann, K. L.; Wheeler, D. R.; Polsky, R.; Brozik, S. M.; Brozik, J. A.; Rudolph, A. R. Liquid-cell scanning transmission electron microscopy and fluorescence correlation spectroscopy of DNA-directed gold nanoparticle assemblies. *Micron* **2019**, *119*, 54−63.
(60) Keskin, S.; Besztejan, S.; Kassier, G. n.; Manz, S.; Bücker, R.; Riekeberg, S.; Trieu, H. K.; Rentmeister, A.; Miller, R. D. Visualization of multimerization and self-assembly of DNA-functionalized gold nanoparticles using in-liquid transmission electron microscopy. *J. Phys. Chem. Lett.* **2015**, *6* (22), 4487−4492.
(61) Kuang, Z.-Y.; Fan, Y.-J.; Tao, L.; Li, M.-L.; Zhao, N.; Wang, P.; Chen, E.-Q.; Fan, F.; Xie, H.-L. Alignment Control of Nematic Liquid Crystal using Gold Nanoparticles Grafted by the Liquid Crystalline Polymer with Azobenzene Mesogens as the Side Chains. *ACS Appl. Mater. Interfaces* **2018**, *10* (32), 27269−27277.
(62) Sutter, E.; Zhang, B.; Sutter, S.; Sutter, P. In situ electron microscopy of the self-assembly of single-stranded DNA-functionalized Au nanoparticles in aqueous solution. *Nanoscale* **2019**, *11* (1), 34−44.
(63) Touve, M. A.; Carlini, A. S.; Gianneschi, N. C. Self-assembling peptides imaged by correlated liquid cell transmission electron microscopy and MALDI-imaging mass spectrometry. *Nat. Commun.* **2019**, *10* (1), 4837.
(64) Elliot, A. J.; Bartels, D. M. *The reaction set, rate constants and g-values for the simulation of the radiolysis of light water over the range 20 deg to 350 deg C based on information available in 2008*; Atomic Energy Canada Limited: Canada, 2009; p 162.
(65) Le Caër, S. Water radiolysis: influence of oxide surfaces on H2 production under ionizing radiation. *Water* **2011**, *3* (1), 235−253.
(66) Guidelli, E. J.; Baffa, O. Influence of photon beam energy on the dose enhancement factor caused by gold and silver nanoparticles: An experimental approach. *Med. Phys.* **2014**, *41* (3), 032101.
(67) Kim, J.-K.; Seo, S.-J.; Kim, H.-T.; Kim, K.-H.; Chung, M.-H.; Kim, K.-R.; Ye, S.-J. Enhanced proton treatment in mouse tumors through proton irradiated nanoradiator effects on metallic nanoparticles. *Phys. Med. Biol.* **2012**, *57* (24), 8309.
(68) Gagnon, W.; Cundiff, J. Dose enhancement from backscattered radiation at tissue−metal interfaces irradiated with high energy electrons. *Br. J. Radiol.* **1980**, *53* (629), 466−470.
(69) Benedetto, J.; Boesch, H.; Oldham, T.; Brown, G. Measurement of low-energy x-ray dose enhancement in MOS devices with metal silicide gates. *IEEE Trans. Nucl. Sci.* **1987**, *34* (6), 1540−1543.
(70) Schulman, S. G. Fundamentals of Interaction of Ionizing Radiations with Chemical, Biochemical, and Pharmaceutical Systems. *J. Pharm. Sci.* **1973**, *62* (11), 1745−1757.
(71) Frias Batista, L. M.; Meader, V. K.; Romero, K.; Kunzler, K.; Kabir, F.; Bullock, A.; Tibbetts, K. M. Kinetic Control of [AuCl4]− Photochemical Reduction and Gold Nanoparticle Size with Hydroxyl Radical Scavengers. *J. Phys. Chem. B* **2019**, *123* (33), 7204−7213.
(72) Jiang, N. Beam damage by the induced electric field in transmission electron microscopy. *Micron* **2016**, *83*, 79−92.
(73) Ahn, C.; Krivanek, O.; Burgner, R.; Disko, M.; Swann, P. *EELS Atlas: A reference collection of electron energy loss spectra covering all stable elements.*; Gatan Inc.: Warrendale, PA, 1983.
(74) Berger, M. J.; Coursey, J. S.; Zucker, M. A.; Chang, J. NIST Standard Reference Database. https://physics.nist.gov/PhysRefData/Star/Text/ESTAR.html (accessed January 6, 2020).
(75) Hufschmid, R.; Teeman, E.; Mehdi, B. L.; Krishnan, K. M.; Browning, N. D. Observing the colloidal stability of iron oxide nanoparticles in situ. *Nanoscale* **2019**, *11* (27), 13098−13107.
(76) Parent, L. R.; Gnanasekaran, K.; Korpanty, J.; Gianneschi, N. C. 100th Anniversary of Macromolecular Science Viewpoint: Polymeric Materials by In Situ Liquid-Phase Transmission Electron Microscopy. *ACS Macro Lett.* **2020**, 14−38.
(77) Yuk, J. M.; Park, J.; Ercius, P.; Kim, K.; Hellebusch, D. J.; Crommie, M. F.; Lee, J. Y.; Zettl, A.; Alivisatos, A. P. High-Resolution EM of Colloidal Nanocrystal Growth Using Graphene Liquid Cells. *Science* **2012**, *336* (6077), 61−64.
(78) Yang, J.; Koo, J.; Kim, S.; Jeon, S.; Choi, B. K.; Kwon, S.; Kim, J.; Kim, B. H.; Lee, W. C.; Lee, W. B.; Lee, H.; Hyeon, T.; Ercius, P.; Park, J. Amorphous-Phase-Mediated Crystallization of Ni Nanocrystals Revealed by High-Resolution Liquid-Phase Electron Microscopy. *J. Am. Chem. Soc.* **2019**, *141* (2), 763−768.
(79) Kim, B. H.; Heo, J.; Kim, S.; Reboul, C. F.; Chun, H.; Kang, D.; Bae, H.; Hyun, H.; Lim, J.; Lee, H. Critical differences in 3D atomic structure of individual ligand-protected nanocrystals in solution. *Science* **2020**, *368* (6486), 60−67.
(80) Jin, B.; Sushko, M. L.; Liu, Z.; Jin, C.; Tang, R. In Situ Liquid Cell TEM Reveals Bridge-Induced Contact and Fusion of Au Nanocrystals in Aqueous Solution. *Nano Lett.* **2018**, *18* (10), 6551−6556.
(81) Patterson, J. P.; Abellan, P.; Denny, M. S.; Park, C.; Browning, N. D.; Cohen, S. M.; Evans, J. E.; Gianneschi, N. C. Observing the Growth of Metal−Organic Frameworks by in Situ Liquid Cell Transmission Electron Microscopy. *J. Am. Chem. Soc.* **2015**, *137* (23), 7322−7328.

https://dx.doi.org/10.1021/acs.nanolett.0c04636
Nano Lett. 2021, 21, 1141−1149